

Predicting Sharp and Accurate Occlusion Boundaries in Monocular Depth Estimation Using Displacement Fields

Michaël Ramamonjisoa^{*,1} Yuming Du^{*,1} Vincent Lepetit¹
 LIGM, IMAGINE, Ecole des Ponts, Univ Gustave Eiffel, ESIEE Paris, CNRS,
 Marne-la-vallée France
 {first.lastname}@enpc.fr

Abstract

Current methods for depth map prediction from monocular images tend to predict smooth, poorly localized contours for the occlusion boundaries in the input image. This is unfortunate as occlusion boundaries are important cues to recognize objects, and as we show, may lead to a way to discover new objects from scene reconstruction. To improve predicted depth maps, recent methods rely on various forms of filtering or predict an additive residual depth map to refine a first estimate. We instead learn to predict, given a depth map predicted by some reconstruction method, a 2D displacement field able to re-sample pixels around the occlusion boundaries into sharper reconstructions. Our method can be applied to the output of any depth estimation method, in an end-to-end trainable fashion. For evaluation, we manually annotated the occlusion boundaries in all the images in the test split of popular NYUv2-Depth dataset. We show that our approach improves the localization of occlusion boundaries for all state-of-the-art monocular depth estimation methods that we could evaluate ([31, 10, 6, 27]), without degrading the depth accuracy for the rest of the images.

1. Introduction

Monocular depth estimation (MDE) aims at predicting a depth map from a single input image. It attracts many interests, as it can be useful for many computer vision tasks and applications, such as scene understanding, robotic grasping, augmented reality, etc. Recently, many methods have been proposed to solve this problem using Deep Learning approaches, either relying on supervised learning [7, 6, 31, 10] or on self-learning [15, 53, 42], and these methods already often obtain very impressive results.

* Authors with equal contribution.

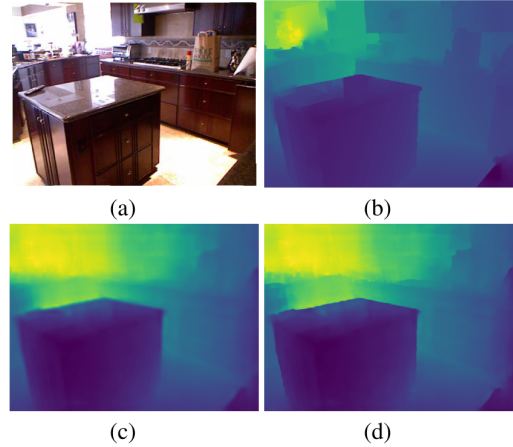


Figure 1. (a) Input image with our occlusion boundary (OB) manual annotation from NYUv2-OC++ in green, (b) Ground truth depth from NYUv2-Depth, (c) Predicted depth using [43], (d) Refined depth using our pixel displacement method.

However, as demonstrated in Fig. 1, despite the recent advances, the occlusion boundaries in the predicted depth maps remain poorly reconstructed. These occlusion boundaries correspond to depth discontinuities happening along the silhouettes of objects [48, 29]. Accurate reconstruction of these contours is thus highly desirable, for example for handling partial occlusions between real and virtual objects in Augmented Reality or more fundamentally, for object understanding, as we show in Fig. 2. We believe that this direction is particularly important: Depth prediction generalizes well to unseen objects and even to unseen object categories, and being able to reconstruct well the occlusion boundaries could be a promising line of research for unsupervised object discovery.

In this work, we introduce a simple method to overcome smooth occlusion boundaries. Our method improves their sharpness as well as their localization in the images. It relies on a differentiable module that takes an initial depth map provided by some depth prediction method, and re-sample

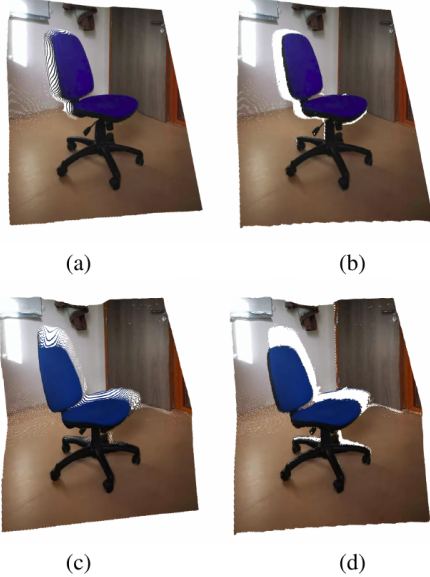


Figure 2. Application of our depth map refinement to 3D object extraction. (a-b) and (c-d) are two point cloud views of our extracted object. The left column shows point clouds extracted from the initially predicted depth image while the right one shows the result after using our depth refinement method. Our method suppresses long tails around object boundaries, as we achieve sharper occlusion boundaries.

it to obtain more accurate occlusion boundaries. Optionally, it can also take the color image as additional input for guidance information and obtain even better contour localization. This is done by training a deep network to predict a 2D displacement field, applied to the initial depth map. This contrasts with previous methods that try to improve depth maps by predicting residual offsets for depth values [26, 59]. We show that predicting displacements instead of such a residual helps reaching sharper occluding boundaries. We believe this is because our module enlarges the family of functions that can be represented by a deep network. As our experiments show, this solution is complementary with all previous solutions as it systematically improves the localization and reconstruction of the occlusion boundaries.

In order to evaluate the occlusion boundary reconstruction performance of existing MDE methods and of our proposed method, we manually annotated the occlusion boundaries in all the images of the NYUv2 test set. Some annotations are shown in Fig. 3 and in the supplementary material. We rely on the metrics introduced in [30] to evaluate the reconstruction and localization accuracy of occlusion boundaries in predicted depth maps. We show that our method quantitatively improves the performance of all state-of-the-art MDE methods in terms of localization accuracy while maintaining or improving the global performance in depth

reconstruction on two benchmark datasets. We will release our annotation dataset NYUv2-OC++ dataset upon publication.

In the rest of the paper, we first discuss related work. We then present our approach to sharpen occlusion boundaries in depth maps. Finally, we describe our experiments and results to prove how our method improves state-of-the-art MDE methods.

2. Related Work

Occlusion boundaries are a notorious and important challenge in dense reconstruction from images, for multiple reasons. For example, it is well known that in the case of stereo reconstruction, some pixels in the neighborhood of occluding boundaries are hidden in one image but visible in the other image, making the task of pixel matching difficult. In this context, numerous solutions have already been proposed to alleviate this problem [11, 24, 28, 13]. We focus here on recent techniques used in monocular depth estimation to improve the reconstruction of occlusion boundaries.

2.1. Deep Learning for Monocular Depth Estimation (MDE) and Occlusion Boundaries

MDE has already been studied thoroughly in the past due to its fundamental and practical importance. The surge of deep learning methods and large scale datasets has helped it improve continuously, with both supervised and self-supervised learning approaches. To tackle the scale ambiguity discussed in MDE discussed in [7], multi-scale deep learning methods have been widely used to learn depth priors as they extract global context from an image [6]. This approach has seen continuous improvement as more sophisticated and deeper architectures [46, 19, 31] were being developed.

Ordinal regression [10] was proposed as an alternative approach to direct depth regression in MDE. This method reached state-of-the-art on both popular MDE benchmarks NYUv2-Depth [47] and KITTI [12] and was later extended [32]. While ordinal regression helps reaching sharper occlusion boundaries, those are unfortunately often inaccurately located in the image, as our experiments show.

Another direction to improve the sharpness of object and occlusion boundaries in MDE is loss function design. L1-loss and variants such as the Huber and BerHu estimators [40, 61] have now been widely adopted instead of L2 since they tend to penalize discontinuities less. However, this solution is not perfect and inaccurate or smooth occlusion boundaries remains [27]. To improve their reconstruction quality, previous work considered depth gradient matching constraints [6] and depth-to-image gradient [20, 15] constraints, however for the latter, occlusion boundaries do not always correspond to strong image gradients, and conversely *e.g.* for areas with texture gradients.

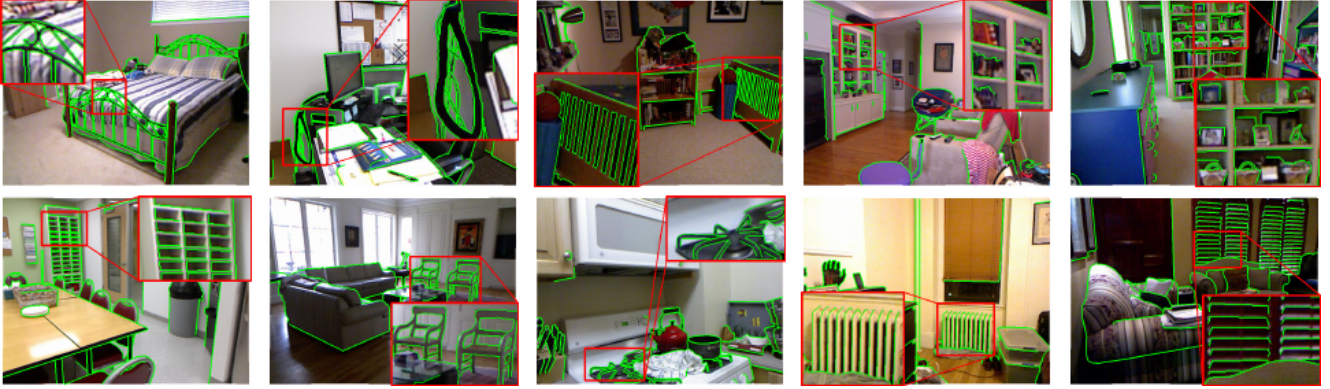


Figure 3. Samples of our NYUv2-OC++ dataset, which extends NYUv2-OC from [43]. The selected highlighted regions in red rectangles display high-quality and fine-grained annotations.

Constraints explicitly based on occlusion boundaries have also been proposed [57, 56, 43], leading to a performance increase in quality of occlusion boundary reconstruction.

Our work is complementary to all of the above approaches, as we show that it can improve the localization and reconstruction of occlusion boundaries in all state-of-the-art deep learning based methods.

2.2. Depth Refinement Methods

In this section we discuss two main approaches that can be used to refine depth maps predictions: We first discuss the formerly popular Conditional Random Fields (CRFs), then classical filtering methods and their newest versions.

Several previous work used CRFs post-processing potential to refine depth maps predictions. These works typically define pixel-wise and pair-wise loss terms between pixels and their neighbors using an intermediate predicted guidance signal such as geometric features [50] or reliability maps [21]. An initially predicted depth map is then refined by performing inference with the CRF, sometimes iteratively or using cascades of CRFs [54, 55]. While most of these methods help improving the initial depth predictions and yield qualitatively more appealing results, those methods still under-perform state-of-the-art non-CRF MDE methods while being more computationally expensive.

Another option for depth refinement is to use image enhancement methods. Even though these methods do not necessarily explicitly target occlusion boundaries, they can be potential alternative solutions to ours.

Bilateral filtering is a popular and currently state-of-the-art method for image enhancement, in particular as a denoising method preserving image contours. Although historically, it was limited for post-processing due to its computational complexity, recent work have successfully made bilateral filters reasonably efficient and fully differentiable [34, 52]. These recent methods have been successful when applied in downsampling-upsampling schemes, but

have not been used yet in the context of MDE. Guided filters [18] have been proposed as an alternative simpler version of the bilateral filter. We show in our experiments that both guided and bilateral filters sharpen occlusion boundaries thanks to their usage of the image for guidance. They however sometime produce false depth gradients artifacts. The bilateral solver [2] formulates the bilateral filtering problem as a regularized least-squares optimization problem, allowing fully differentiable and much faster computation. However, we show in our experiments that our end-to-end trainable method compares favorably against this method, both in speed and accuracy.

2.3. Datasets with Image Contours

Several datasets of image contours or occlusion boundaries already exists. Popular datasets for edge detection training and evaluation were focused on perceptual [39, 38, 1] or object instance [8] boundaries. However, those datasets often lack annotation of the occlusion relationship between two regions separated by the boundaries. Other datasets [45, 23, 22, 51] annotated occlusion relationship between objects, however they do not contain ground truth depth.

The NYUv2-Depth dataset [47] is a popular MDE benchmark which provides such depth ground truth. Several methods for instance boundary detection have benefited from this depth information [16, 5, 44, 17, 4] to improve their performances on object instance boundaries detection.

The above cited datasets all lack object self-occlusion boundaries and are sometimes inaccurately annotated. Our NYUv2-OC++ dataset provides manual annotations for the occlusion boundaries on top of NYUv2-Depth for all of its 654 test images. As discussed in [43], even though it is a tedious task, manual annotation is much more reliable than automated annotation that could be obtained from depth maps. Fig. 3 illustrates the extensive and accurate coverage of the occlusion boundaries of our annotations. This

dataset enables simultaneous evaluation of depth estimation methods and occlusion boundary reconstruction as the 100 images iBims dataset [30], but is larger and has been widely used for MDE evaluation.

3. Method

In this section, we introduce our occlusion boundary refinement method as follows. Firstly, we present our prior hypothesis on the distribution of depth map pixels around occlusion boundaries and derive a model to shrink this distribution. We then prove our hypothesis using an hand-crafted method. Based on this model, we propose an end-to-end trainable module which can resample pixels of an input depth image to restore its sharp occlusion boundaries.

3.1. Prior Hypothesis

Occlusion boundaries correspond to regions in the image where depth exhibits large and sharp variations, while the other regions tend to vary much smoother. Due to the small proportion of such sharp regions, neural networks tend to predict over-smoothed depths in the vicinity of occlusion boundaries.

We show in this work that sharp and accurately located boundaries can be recovered by resampling pixels in the depth map. This resampling can be formalized as:

$$\forall \mathbf{p} \in \Omega, \quad D(\mathbf{p}) \leftarrow D(\mathbf{p} + \delta \mathbf{p}(\mathbf{p})), \quad (1)$$

where D is a depth map, \mathbf{p} denotes an image location in domain Ω , and $\delta \mathbf{p}(\mathbf{p})$ a 2D displacement that depends on \mathbf{p} . This formulation allows the depth values on the two sides of occlusion boundaries to be “stitched” together and replace the over-smoothed depth values.

Another option to improve depth values would be to predict a residual depth, which can be formalized as, for comparison:

$$\forall \mathbf{p} \in \Omega, \quad D(\mathbf{p}) \leftarrow D(\mathbf{p}) + \Delta D(\mathbf{p}). \quad (2)$$

We argue that updating the predicted depth \hat{D} using predicted pixel shifts to recover sharp occlusion boundaries in depth images works better than predicting the residual depth. We validate this claim with the experiments presented below on toy problems, and on real predicted depth maps in Section 4.

3.2. Testing the Optimal Displacements

To first validate our assumption that a displacement field $\delta \mathbf{p}(\mathbf{p})$ can improve the reconstructions of occlusion boundaries, we estimate the optimal displacements using ground truth depth for several predicted depth maps as:

$$\forall \mathbf{p} \in \Omega, \delta \mathbf{p}^* = \arg \min_{\delta \mathbf{p}: \mathbf{p} + \delta \mathbf{p} \in \mathcal{N}(\mathbf{p})} (D(\mathbf{p}) - \hat{D}(\mathbf{p} + \delta \mathbf{p}))^2. \quad (3)$$

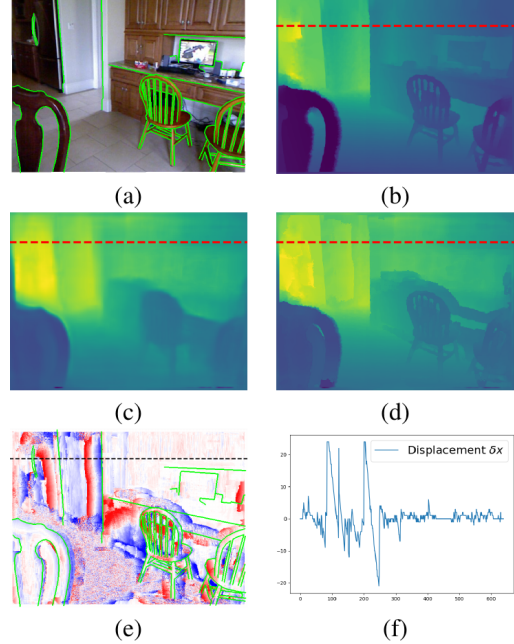


Figure 4. Refinement results using the method described in Section 3.1 to recover the optimal displacement field (best seen in color). (a) is the input RGB image with superimposed NYUv2-OC++ annotation in green and (b) its associated Ground Truth depth. (c) is the prediction using [31] with pixel displacements $\delta \mathbf{p}$ from Eq. (3) and (d) the refined prediction. (e) is the horizontal component of the displacement field $\delta \mathbf{p}^*$ obtained by Eq. (3). Red and blue color indicate positive and negative values respectively. (f) is the horizontal component δx of displacement field $\delta \mathbf{p}^*$ along the dashed red line drawn in (b-e).

In words, solving this problem is equivalent to finding for each pixel the optimal displacement $\delta \mathbf{p}^*$ that reconstructs the ground truth depth map D from a predicted depth map \hat{D} . We solve Eq. (3) by performing for all pixels \mathbf{p} an exhaustive search of $\delta \mathbf{p}$ within a neighborhood $\mathcal{N}(\mathbf{p})$ of size 50×50 . Qualitative results are shown in Fig. 4. The depth map obtained by applying this optimal displacement field is clearly much better.

In practice, we will have to predict the displacement field to apply this idea. This is done by training a deep network, which is detailed in the next subsection. We then check on a toy problem that this yields better performance than predicting residual depth with a deep network of similar capacity.

3.3. Method Overview

Based on our model, we propose to learn the displacements of pixels in predicted depth images using CNNs. Our approach is illustrated in Fig. 6: Given a predicted depth image \hat{D} , our network predicts a displacement field $\delta \mathbf{p}$ to resample the image locations in depth map \hat{D} according to Eq. (1). This approach can be implemented as a Spatial

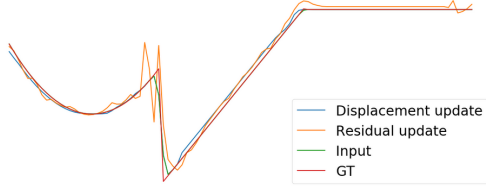


Figure 5. Comparison between displacement and residual update learning. Both residual and displacement learning can predict sharper edges, however residual updates often produce artifacts along the edges while displacements update does not.

Transformer Network [25].

Image guidance can be helpful to improve the occlusion boundary precision in refined depth maps and can also help to discover edges that were not visible in the initial predicted depth map \hat{D} . However, it should be noted that our network can still work even without image guidance.

3.4. Training Our Model on Toy Problems

In order to verify that displacement fields δp presented in Section 3.1 can be learned, we first define a toy problem in 1D.

In this toy problem, as shown in Fig. 1, we model the signals D to be recovered as piecewise continuous functions, generated as sequences of basic functions such as step, affine and quadratic functions. These samples exhibit strong discontinuities at junctions and smooth variations everywhere else, which is a property similar to real depth maps. We then convolve the D signals with random-size (blurring) Gaussian kernels to obtain smooth versions \hat{D} . This gives us a training set \mathcal{T} of (\hat{D}, D) pairs.

We use \mathcal{T} to train a network $f(\cdot; \Theta_f)$ of parameters to predict a displacement field:

$$\min_{\Theta_f} \sum_{(\hat{D}, D) \in \mathcal{T}} \sum_{\mathbf{p}} \|D(\mathbf{p}) - \hat{D}(\mathbf{p} + f(\hat{D}; \Theta_f)(\mathbf{p}))\|_2^2. \quad (4)$$

and a network $g(\cdot; \Theta_g)$ of parameters to predict a residual depth map:

$$\min_{\Theta_g} \sum_{(\hat{D}, D) \in \mathcal{T}} \sum_{\mathbf{p}} (D(\mathbf{p}) - \hat{D}(\mathbf{p}) + g(\hat{D}; \Theta_g)(\mathbf{p}))^2. \quad (5)$$

As shown in Fig. 5, we found that predicting a residual update produces severe artifacts around edges such as overshooting effects. We argue that these issues arise because the residual CNN g is also trained on regions where the values of \hat{D} and D are different even away from edges, thus encouraging network g to also correct these regions. By contrast, our method does not create such overshooting effects as it does not alter the local range of values around edges.

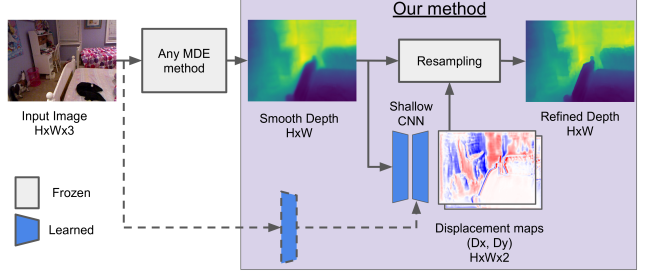


Figure 6. Our proposed pipeline for depth edge sharpening. The dashed lines define the optional guidance with RGB features for our shallow network.

It is worth noticing that even when we allow x and y to have slightly different values in non-edge areas -which simulates residual error between predicted and ground truth depth-, our method still converges to a good solution, compared to the residual CNN.

We extend our approach validation from 1D to 2D, where the 1D signal is replaced by 2D images with different polygons of different values. We apply the same operation to smooth the images and then use our network to recover the original sharp images from the smooth ones. We observed similar results in 2D: residual CNN always generate artifacts in refined predictions. Some results of our 2D toy problem can be found in supplementary material.

3.5. Learning to Sharpen Depth Predictions

To learn to produce sharper depth predictions using displacement fields, we first trained our method in a similar fashion to the toy problem described in subsection 3.4. While this already improves the quality of occlusion boundaries of all depth map predictions, we show that we can further improve quantitative results by training our method end-to-end on top of MDE methods as presented in Fig 6.

4. Experiments

In this section, we first detail our implementation, describe the metrics we use to evaluate the reconstruction of the occlusion boundaries and the accuracy of the depth prediction, and then present the results of the evaluations of our method on the outputs from different MDE methods.

4.1. Implementation Details

We implemented our network using the Pytorch [41] framework. We trained it on the output of a MDE method [43], using Adam optimization with an initial learning rate of $5e-4$ and weight decay of $1e-6$, and the *poly* learning rate policy [60], during 32k iterations on NYUv2 [47]. This dataset contains 1449 pairs RGB and depth images, split into 795 samples for training and 654 for testing. Batch size was set to 1. The input images were

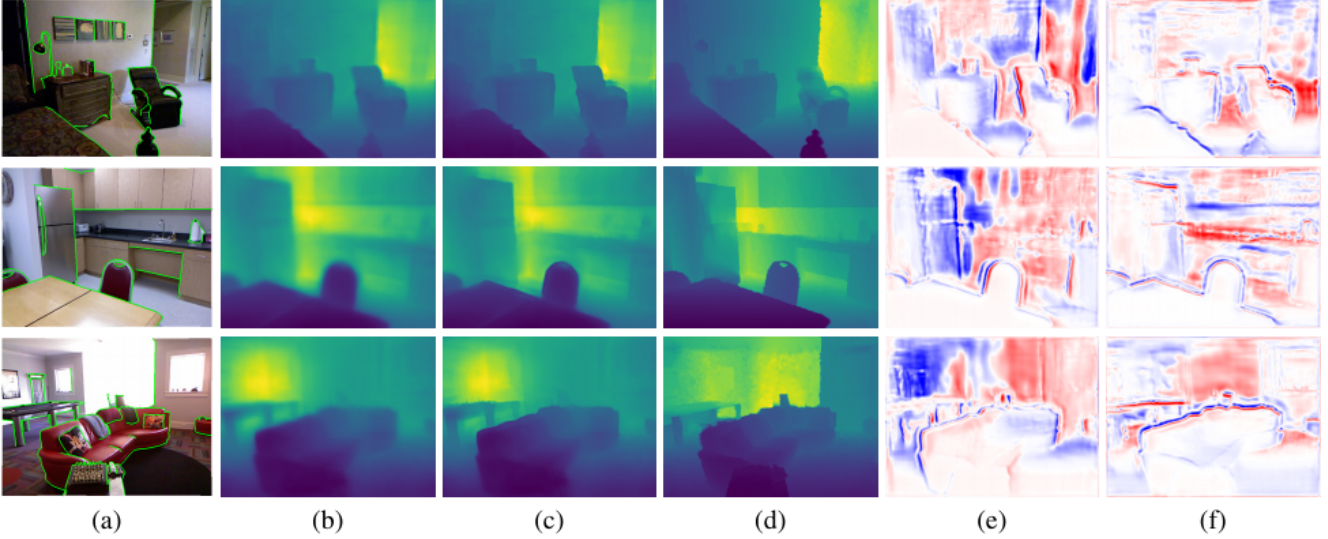


Figure 7. Refinement results using our method (best seen in color). From left to right: (a) input RGB image with NYUv2-OC++ annotation in green, (b) SharpNet [43] depth prediction, (c) Refined prediction, (d) Ground truth depth, (e) Horizontal and (f) Vertical components of the displacement field. Displacement fields are clipped between ± 15 pixels. Although SharpNet is used as an example here because it is currently state-of-the-art on occlusion boundary accuracy, similar results can be observed when refining predictions from other methods.

resized with scales $[0.75, 1, 1, 5, 2]$ and then cropped and padded to 320×320 .

4.2. Evaluation metrics

4.2.1 Evaluation of monocular depth prediction

As for previous work [7, 6, 31], we evaluate the monocular depth predictions using the following metrics: Root Mean Squared linear Error (RMSE(lin)), mean absolute relative error (rel), mean \log_{10} error (\log_{10}), Root Mean Squared log Error (RMSE(log)), and the accuracy under threshold ($\sigma_i < 1.25^i$, $i = 1, 2, 3$).

4.2.2 Evaluation of occlusion boundary accuracy

Following the work of Koch *et al.* [30], we evaluate the accuracy of occlusion boundaries using the proposed depth boundary errors, which evaluates the accuracy ϵ_{acc} and completion ϵ_{comp} of predicted occlusion boundaries. The boundaries are first extracted using a Canny edge detector [3] with predefined thresholds on a normalized predicted depth image. As illustrated in Fig. 8, ϵ_{acc} is taken as the average Chamfer distance in pixels [9] from the predicted boundaries to the ground truth boundaries; ϵ_{com} is taken as the average Chamfer distance from ground truth boundaries to the predicted boundaries.

4.3. Evaluation on the NYUv2 Dataset

We evaluate our method by refining the predictions of different state-of-the-art methods [7, 31, 10, 43, 27, 58].



Figure 8. Occlusion boundary evaluation metrics based on the Chamfer distance, as introduced in [30]. The blue lines represent the ground truth boundaries, the red curve the predicted boundary. Only the boundaries in the green area are taken into account during the evaluation of accuracy (a), and only the yellow area are taken into account during the evaluation of completeness (b). (a) The accuracy is evaluated from the distances of points on the predicted boundaries to the ground truth boundaries. (b) The completeness is evaluated from the distances of points on the ground truth boundaries to the predicted boundaries.

Our network is trained using the 795 labeled NYUv2 depth images of training dataset with corresponding RGB images as guidance. To enable a fair comparison, we evaluate only pixels inside the crop defined in [7] for all methods. Table 1 shows the evaluation of refined predictions of different methods using our network. With the help of our proposed network, the occlusion boundary accuracy of all methods can be largely improved, without degrading the global depth estimation accuracy. We also show qualitative results of our refinement method in Fig. 7.

4.4. Evaluation on the iBims Dataset

We applied our method trained on NYUv2 dataset to refine the predictions from various methods [7, 6, 31, 36, 33,

| Method | Refine | Depth error (\downarrow) | | | | Depth accuracy (\uparrow) | | | Occlusion Boundaries (\downarrow) | |
|-------------------------------|--------|------------------------------|--------------|--------------|--------------|-------------------------------|--------------|--------------|---------------------------------------|-------------------|
| | | rel | \log_{10} | RMSE (lin) | RMSE (log) | σ_1 | σ_2 | σ_3 | ϵ_{acc} | ϵ_{comp} |
| Eigen <i>et al.</i> [7] | - | 0.234 | 0.095 | 0.760 | 0.265 | 0.612 | 0.886 | 0.971 | 9.936 | 9.997 |
| | ✓ | 0.232 | 0.094 | 0.758 | 0.263 | 0.615 | 0.889 | 0.971 | 2.168 | 8.173 |
| Laina <i>et al.</i> [31] | - | 0.142 | 0.059 | 0.510 | 0.181 | 0.818 | 0.955 | 0.988 | 4.702 | 8.982 |
| | ✓ | 0.140 | 0.059 | 0.509 | 0.180 | 0.819 | 0.956 | 0.989 | 2.372 | 7.041 |
| Fu <i>et al.</i> [10] | - | 0.131 | 0.053 | 0.493 | 0.174 | 0.848 | 0.956 | 0.984 | 3.872 | 8.117 |
| | ✓ | 0.136 | 0.054 | 0.502 | 0.178 | 0.844 | 0.954 | 0.983 | 3.001 | 7.242 |
| Ramamonjisoa and Lepetit [43] | - | 0.116 | 0.053 | 0.448 | 0.163 | 0.853 | 0.970 | 0.993 | 3.041 | 8.692 |
| | ✓ | 0.117 | 0.054 | 0.457 | 0.165 | 0.848 | 0.970 | 0.993 | 1.838 | 6.730 |
| Jiao <i>et al.</i> [27] | - | 0.093 | 0.043 | 0.356 | 0.134 | 0.908 | 0.981 | 0.995 | 8.730 | 9.864 |
| | ✓ | 0.092 | 0.042 | 0.352 | 0.132 | 0.910 | 0.981 | 0.995 | 2.410 | 8.230 |
| Yin <i>et al.</i> [58] | - | 0.112 | 0.047 | 0.417 | 0.144 | 0.880 | 0.975 | 0.994 | 1.854 | 7.188 |
| | ✓ | 0.112 | 0.047 | 0.419 | 0.144 | 0.879 | 0.975 | 0.994 | 1.762 | 6.307 |

Table 1. Evaluation of our method on the output of several state-of-the-art methods on NYUv2. Our method significantly improves the occlusion boundaries metrics ϵ_{acc} and ϵ_{comp} without degrading the other metrics related to the overall depth accuracy. These results were computed using available depth maps predictions (apart from Jiao *et al.* [27] who sent us their predictions) within cropped region proposed in [7].

35, 43] on the iBims dataset [30]. Table 2 shows that our network significantly improves the accuracy and completeness metrics for the occluding boundaries of all predictions on this dataset as well.

4.5. Comparison with Other Methods

To demonstrate the efficiency of our proposed method, we compare our method with existing filtering methods [49, 18, 2, 52]. We use the prediction of [7] as input, and compare the accuracy of depth estimation and occlusion boundaries of each method. Note that for the filters with hyper-parameters, we tested each filter with a series of hyper-parameters and select the best refined results. For the fast bilateral solver [2] and the deep guided filter [52], we use its default settings from the official implementation. We keep the same network with and without deep guided filter, and train both times with the same learning rate and data augmentation. As shown in Table 3, our method achieves the best accuracy for occlusion boundaries. We argue that the performance of the deep guided filter is lower due to generated artifacts which are discussed in Section 3.4.

4.6. Influence of the Loss Function and the Guidance Image

In this section, we report several ablation studies to analyze the favorable factors of our network in terms of performances. Fig. 6 shows the architecture of our baseline network. All the following networks are trained using the same setting detailed in Section 4.1 and trained on the official 795 RGB-D images of the NYUv2 training set. To evaluate the effectiveness of our method, we choose the predictions of [7] as input, but note that the conclusion is still valid with other MDE methods. Please see supplementary material for

further results.

4.6.1 Loss Functions for Depth Prediction

In Table 4, we show the influence of different loss functions. We apply the Pytorch official implementation of l_1 , l_2 , and the Huber loss. The Disparity loss supervises the network with the reciprocal of depth, the target depth y_{target} is defined as $y_{target} = M/y_{original}$, where M here represents the maximum of depth in the scene. As shown in Table 4, our network trained with l_1 loss achieves the best accuracy for the occlusion boundaries.

4.6.2 Guidance image

We explore the influence of different types of guidance image. The features of guidance images are extracted using an encoder with the same architecture as the depth encoder, except that Leaky ReLU [37] activations are all replaced by standard ReLU [14]. We perform feature fusion of guidance and depth features using skip connections and concatenations of features from the guidance and depth decoder respectively at similar scales.

Table 5 shows the influence of different choices for the guidance image. The edge images are created by accumulating the detected edges using a series of Canny detector with different thresholds. As shown in Table 5, using the original RGB image as guidance achieves the highest accuracy, while using the image converted to grayscale achieves the lowest accuracy, as information is lost during the conversion. Using the Canny edge detector can help to alleviate this problem, as the network achieves better results when switching from gray image to binary edge maps.

| Method | Refine | Depth error (\downarrow) | | | Depth accuracy (\uparrow) | | | Occlusion Boundaries (\downarrow) | |
|--------------------------------|--------|------------------------------|-------------------|-------------|-------------------------------|-------------|-------------|---------------------------------------|-------------------|
| | | rel | log ₁₀ | RMSE (lin) | σ_1 | σ_2 | σ_3 | ϵ_{acc} | ϵ_{comp} |
| Eigen <i>et al.</i> [7] | - | 0.32 | 0.17 | 1.55 | 0.36 | 0.65 | 0.84 | 9.97 | 9.99 |
| | ✓ | 0.32 | 0.17 | 1.54 | 0.37 | 0.66 | 0.85 | 4.83 | 8.78 |
| Eigen and Fergus (AlexNet) [6] | - | 0.30 | 0.15 | 1.38 | 0.40 | 0.73 | 0.88 | 4.66 | 8.68 |
| | ✓ | 0.30 | 0.15 | 1.37 | 0.41 | 0.73 | 0.88 | 4.10 | 7.91 |
| Eigen and Fergus (VGG) [6] | - | 0.25 | 0.13 | 1.26 | 0.47 | 0.78 | 0.93 | 4.05 | 8.01 |
| | ✓ | 0.25 | 0.13 | 1.25 | 0.48 | 0.78 | 0.93 | 3.95 | 7.57 |
| Laina <i>et al.</i> [31] | - | 0.26 | 0.13 | 1.20 | 0.50 | 0.78 | 0.91 | 6.19 | 9.17 |
| | ✓ | 0.25 | 0.13 | 1.18 | 0.51 | 0.79 | 0.91 | 3.32 | 7.15 |
| Liu <i>et al.</i> [36] | - | 0.30 | 0.13 | 1.26 | 0.48 | 0.78 | 0.91 | 2.42 | 7.11 |
| | ✓ | 0.30 | 0.13 | 1.26 | 0.48 | 0.77 | 0.91 | 2.36 | 7.00 |
| Li <i>et al.</i> [33] | - | 0.22 | 0.11 | 1.09 | 0.58 | 0.85 | 0.94 | 3.90 | 8.17 |
| | ✓ | 0.22 | 0.11 | 1.10 | 0.58 | 0.84 | 0.94 | 3.43 | 7.19 |
| Liu <i>et al.</i> [35] | - | 0.29 | 0.17 | 1.45 | 0.41 | 0.70 | 0.86 | 4.84 | 8.86 |
| | ✓ | 0.29 | 0.17 | 1.47 | 0.40 | 0.69 | 0.86 | 2.78 | 7.65 |
| Ramamonjisoa and Lepetit [43] | - | 0.27 | 0.11 | 1.08 | 0.59 | 0.83 | 0.93 | 3.69 | 7.82 |
| | ✓ | 0.27 | 0.11 | 1.08 | 0.59 | 0.83 | 0.93 | 2.13 | 6.33 |

Table 2. Refined results of different predictions on iBims

| Method | Depth error (\downarrow) | | | | Depth accuracy (\uparrow) | | | OB (\downarrow) | |
|-------------------------|------------------------------|--------------|--------------|--------------|-------------------------------|--------------|--------------|---------------------|-------------------|
| | rel | log10 | RMSE (lin) | RMSE (log) | σ_1 | σ_2 | σ_3 | ϵ_{acc} | ϵ_{comp} |
| Baseline [7] | 0.234 | 0.095 | 0.766 | 0.265 | 0.610 | 0.886 | 0.971 | 9.926 | 9.993 |
| Bilateral Filter [49] | 0.236 | 0.095 | 0.765 | 0.265 | 0.611 | 0.887 | 0.971 | 9.313 | 9.940 |
| Guided Filter [18] | 0.237 | 0.095 | 0.767 | 0.265 | 0.610 | 0.885 | 0.971 | 6.106 | 9.617 |
| Bilateral Solver [2] | 0.236 | 0.095 | 0.765 | 0.264 | 0.611 | 0.887 | 0.971 | 5.428 | 9.454 |
| Deep Guided Filter [52] | 0.306 | 0.116 | 0.917 | 0.362 | 0.508 | 0.823 | 0.948 | 4.318 | 9.597 |
| Our Method | 0.232 | 0.094 | 0.757 | 0.263 | 0.615 | 0.889 | 0.971 | 2.302 | 8.347 |

Table 3. Comparison with existing methods for image enhancement, adapted to the depth map prediction problems. Our method performs the best for this problem over all the different metrics (\downarrow : Lower is better; \uparrow : Higher is better).

| Method | Depth error (\downarrow) | | | | Depth accuracy (\uparrow) | | | OB (\downarrow) | |
|--------------|------------------------------|-------|--------------|------------|-------------------------------|------------|--------------|---------------------|-------------------|
| | rel | log10 | RMSE (lin) | RMSE (log) | σ_1 | σ_2 | σ_3 | ϵ_{acc} | ϵ_{comp} |
| Baseline [7] | 0.234 | 0.095 | 0.766 | 0.265 | 0.610 | 0.886 | 0.971 | 9.926 | 9.993 |
| l_1 | 0.232 | 0.094 | 0.758 | 0.263 | 0.615 | 0.889 | 0.971 | 2.168 | 8.173 |
| l_2 | 0.232 | 0.094 | 0.757 | 0.263 | 0.615 | 0.889 | 0.971 | 2.302 | 8.347 |
| Huber | 0.232 | 0.095 | 0.758 | 0.263 | 0.615 | 0.889 | 0.972 | 2.225 | 8.282 |
| Disparity | 0.234 | 0.095 | 0.761 | 0.264 | 0.613 | 0.888 | 0.971 | 2.312 | 8.353 |

Table 4. Evaluation of different loss functions for learning the displacement field. The l_1 norm yields the best results.

5. Conclusion

We showed in this paper that by predicting a displacement field to resample depth maps, we can significantly improve the reconstruction accuracy and the localization of occlusion boundaries of any existing method for monocular depth prediction. To evaluate our method, we also intro-

| Method | Depth error (\downarrow) | | | | Depth accuracy (\uparrow) | | | OB (\downarrow) | |
|--------------|------------------------------|-------|------------|------------|-------------------------------|------------|------------|---------------------|-------------------|
| | rel | log10 | RMSE (lin) | RMSE (log) | σ_1 | σ_2 | σ_3 | ϵ_{acc} | ϵ_{comp} |
| Baseline [7] | 0.234 | 0.095 | 0.760 | 0.265 | 0.612 | 0.886 | 0.971 | 9.936 | 9.997 |
| Gray | 0.232 | 0.094 | 0.757 | 0.263 | 0.615 | 0.889 | 0.972 | 2.659 | 8.681 |
| Binary Edges | 0.232 | 0.094 | 0.757 | 0.263 | 0.615 | 0.889 | 0.972 | 2.466 | 8.483 |
| RGB | 0.232 | 0.094 | 0.758 | 0.263 | 0.615 | 0.889 | 0.971 | 2.168 | 8.173 |

Table 5. Evaluation of different ways of using the input image for guidance. Simply using the original color image works best.

duce a new dataset of precisely labeled occlusion boundaries. Beyond evaluation of occlusion boundary reconstruction, this dataset should be extremely valuable for future methods to learn to detect more precisely occlusion boundaries, and we will release it upon publication.

References

- [1] P. Arbelaez, M. Maire, C. Fowlkes, and J. Malik. Contour Detection and Hierarchical Image Segmentation. *PAMI*, 33(5):898–916, 2011. 3
- [2] J.T. Barron and B. Poole. The Fast Bilateral Solver. In *ECCV*, 2016. 3, 7, 8
- [3] J. Canny. A Computational Approach to Edge Detection. *PAMI*, 8(6), 1986. 6
- [4] R. Deng, C. Shen, S. Liu, H. Wang, and X. Liu. Learning to Predict Crisp Boundaries. In *ECCV*, 2018. 3
- [5] Piotr Dollár and C. Lawrence Zitnick. Structured Forests for Fast Edge Detection. In *ICCV*, 2013. 3
- [6] D. Eigen and R. Fergus. Predicting Depth, Surface Normals and Semantic Labels with a Common Multi-Scale Convolutional Architecture. In *ICCV*, 2015. 1, 2, 6, 7, 8

- [7] D. Eigen, C. Puhrsch, and R. Fergus. Depth Map Prediction from a Single Image Using a Multi-Scale Deep Network. In *NIPS*, 2014. 1, 2, 6, 7, 8
- [8] M. Everingham, L. Van Gool, C.K.I. Williams, J. M. Winn, and A. Zisserman. The Pascal Visual Object Classes (VOC) Challenge. *IJCV*, 88(2):303–338, 2010. 3
- [9] H. Fan, H. Su, and L. J. Guibas. A Point Set Generation Network for 3D Object Reconstruction from a Single Image. In *CVPR*, 2017. 6
- [10] H. Fu, A. M. Gong, C. Wang, K. Batmanghelich, and D. Tao. Deep Ordinal Regression Network for Monocular Depth Estimation. In *CVPR*, 2018. 1, 2, 6, 7
- [11] P. Fua. Combining Stereo and Monocular Information to Compute Dense Depth Maps That Preserve Depth Discontinuities. In *IJCAI*, pages 1292–1298, August 1991. 2
- [12] A. Geiger, P. Lenz, C. Stiller, and R. Urtasun. Vision Meets Robotics: the KITTI Dataset. *International Journal of Robotics Research*, 2013. 2
- [13] D. Geiger, B. Ladendorff, and A. Yuille. Occlusions and Binocular Stereo. *IJCV*, 14:211–226, 1995. 2
- [14] X. Glorot, A. Bordes, and Y. Bengio. Deep Sparse Rectifier Neural Networks. In *International Conference on Artificial Intelligence and Statistics*, 2011. 7
- [15] C. Godard, O. Mac Aodha, and G. J. Brostow. Unsupervised Monocular Depth Estimation with Left-Right Consistency. In *CVPR*, 2017. 1, 2
- [16] S. Gupta, P. Arbelaz, and J. Malik. Perceptual Organization and Recognition of Indoor Scenes from RGB-D Images. In *CVPR*, 2013. 3
- [17] S. Gupta, R. Girshick, P. Arbelaz, and J. Malik. Learning Rich Features from RGB-D Images for Object Detection and Segmentation. In *ECCV*, 2014. 3
- [18] K. He, J. Sun, and X. Tang. Guided Image Filtering. *PAMI*, 35:1397–1409, 06 2013. 3, 7, 8
- [19] K. He, X. Zhang, S. Ren, and J. Sun. Deep Residual Learning for Image Recognition. In *CVPR*, 2016. 2
- [20] P. Heise, S. Klose, B. Jensen, and A. Knoll. PM-Huber: Patchmatch with Huber Regularization for Stereo Matching. In *ICCV*, 2013. 2
- [21] M. Heo, J. Lee, K.-R. Kim, H.-U. Kim, and C.-S. Kim. Monocular Depth Estimation Using Whole Strip Masking and Reliability-Based Refinement. In *ECCV*, 2018. 3
- [22] D. Hoiem, A.A. Efros, and M. Hebert. Recovering Occlusion Boundaries from an Image. *IJCV*, 91(3), 2011. 3
- [23] D. Hoiem, A. A. Efros, and M. Hebert. Recovering Surface Layout from an Image. *IJCV*, 75(1):151–172, October 2007. 3
- [24] S.S. Intille and A.F. Bobick. Disparity-Space Images and Large Occlusion Stereo. In *ECCV*, 1994. 2
- [25] M. Jaderberg, K. Simonyan, A. Zisserman, and K. Kavukcuoglu. Spatial Transformer Networks. In *NIPS*, 2015. 5
- [26] J. Jeon and S. Lee. Reconstruction-Based Pairwise Depth Dataset for Depth Image Enhancement Using CNN. In *ECCV*, 2018. 2
- [27] J. Jiao, Y. Cao, Y. Song, and R. W. H. Lau. Look Deeper into Depth: Monocular Depth Estimation with Semantic Booster and Attention-Driven Loss. In *ECCV*, 2018. 1, 2, 6, 7
- [28] T. Kanade and M. Okutomi. A Stereo Matching Algorithm with an Adaptive Window: Theory and Experiment. *PAMI*, 16(9):920–932, September 1994. 2
- [29] K. Karsch, Z. Liao, J. Rock, J. T. Barron, and D. Hoiem. Boundary Cues for 3D Object Shape Recovery. In *CVPR*, 2013. 1
- [30] T. Koch, L. Liebel, F. Fraundorfer, and M. Körner. Evaluation of CNN-Based Single-Image Depth Estimation Methods. In *ECCV*, 2018. 2, 4, 6, 7
- [31] I. Laina, C. Rupprecht, V. Belagiannis, F. Tombari, and N. Navab. Deeper Depth Prediction with Fully Convolutional Residual Networks. In *3DV*, 2016. 1, 2, 4, 6, 7, 8
- [32] J.-H. Lee and C.-S. Kim. Monocular Depth Estimation Using Relative Depth Maps. In *CVPR*, June 2019. 2
- [33] J. Li, R. Klein, and A. Yao. A Two-Streamed Network for Estimating Fine-Scaled Depth Maps from Single RGB Images. In *ICCV*, 2017. 7, 8
- [34] Y. Li, J.-B. Huang, N. Ahuja, and M.-H. Yang. Deep Joint Image Filtering. In *ECCV*, 2016. 3
- [35] C. Liu, J. Yang, D. Ceylan, E. Yumer, and Y. Furukawa. PlaneNet: Piece-Wise Planar Reconstruction from a Single RGB Image. In *CVPR*, 2018. 7, 8
- [36] F. Liu, C. Shen, and G. Lin. Deep Convolutional Neural Fields for Depth Estimation from a Single Image. In *CVPR*, 2015. 7, 8
- [37] A. L. Maas, A. Y. Hannun, and A. Y. Ng. Rectifier Nonlinearities Improve Neural Network Acoustic Models. In *ICML*, 2013. 7
- [38] D. Martin, C. Fowlkes, and J. Malik. Learning to Detect Natural Image Boundaries Using Local Brightness, Color and Texture Cues. *PAMI*, 26(5), 2004. 3
- [39] D. Martin, C. Fowlkes, D. Tal, and J. Malik. A Database of Human Segmented Natural Images and Its Application to Evaluating Segmentation Algorithms and Measuring Ecological Statistics. In *ICCV*, 2001. 3
- [40] B. Owen. A Robust Hybrid of Lasso and Ridge Regression. *Contemp. Math.*, 443, 2007. 2
- [41] A. Paszke, S. Gross, S. Chintala, G. Chanan, E. Yang, Z. DeVito, Z. Lin, A. Desmaison, L. Antiga, and A. Lerer. Automatic Differentiation in Pytorch. In *NIPS Workshop*, 2017. 5
- [42] M. Poggi, A. F. Tosi, and S. Mattoccia. Learning Monocular Depth Estimation with Unsupervised Trinocular Assumptions. In *3DV*, pages 324–333, 2018. 1
- [43] M. Ramamonjisoa and V. Lepetit. Sharpnet: Fast and Accurate Recovery of Occluding Contours in Monocular Depth Estimation. In *ICCV Workshop*, 2019. 1, 3, 5, 6, 7, 8
- [44] X. Ren and L. Bo. Discriminatively Trained Sparse Code Gradients for Contour Detection. In *NIPS*, 2012. 3
- [45] X. Ren, C.C. Fowlkes, and J. Malik. Figure/ground Assignment in Natural Images. In *ECCV*, 2006. 3
- [46] O. Ronneberger, P. Fischer, and T. Brox. U-Net: Convolutional Networks for Biomedical Image Segmentation. In *MICCAI*, 2015. 2
- [47] N. Silberman, D. Hoiem, P. Kohli, and R. Fergus. Indoor Segmentation and Support Inference from RGBD Images. In *ECCV*, 2012. 2, 3, 5

- [48] R. Szeliski and R. Weiss. Robust Shape Recovery from Occluding Contours Using a Linear Smoother. *IJCV*, 28(1):27–44, 1998. 1
- [49] C. Tomasi and R. Manduchi. Bilateral Filtering for Gray and Color Images. In *ICCV*, 1998. 7, 8
- [50] P. Wang, X. Shen, B. Russell, S. Cohen, B. Price, and A. L. Yuille. SURGE: Surface Regularized Geometry Estimation from a Single Image. In *NIPS*, 2016. 3
- [51] P. Wang and A. Yuille. DOC: Deep Occlusion Estimation from a Single Image. In *ECCV*, 2016. 3
- [52] H. Wu, S. Zheng, J. Zhang, and K. Huang. Fast End-To-End Trainable Guided Filter. In *CVPR*, 2018. 3, 7, 8
- [53] J. Xie, R. B. Girshick, and A. Farhadi. Deep3D: Fully Automatic 2D-To-3d Video Conversion with Deep Convolutional Neural Networks. In *ECCV*, 2016. 1
- [54] D. Xu, E. Ricci, W. Ouyang, X. Wang, and N. Sebe. Multi-Scale Continuous CRFs as Sequential Deep Networks for Monocular Depth Estimation. In *CVPR*, 2017. 3
- [55] D. Xu, E. Ricci, W. Ouyang, X. Wang, and N. Sebe. Monocular Depth Estimation Using Multi-Scale Continuous CRFs as Sequential Deep Networks. *PAMI*, 2018. 3
- [56] Z. Yang, P. Wang, Y. Wang, W. Xu, and R. Nevatia. LEGO: Learning Edge with Geometry All at Once by Watching Videos. In *CVPR*, 2018. 3
- [57] Z. Yang, W. Xu, L. Zhao, and R. Nevatia. Unsupervised Learning of Geometry from Videos with Edge-Aware Depth-Normal Consistency. In *AAAI*, 2018. 3
- [58] W. Yin, Y. Liu, C. Shen, and Y. Yan. Enforcing Geometric Constraints of Virtual Normal for Depth Prediction. In *ICCV*, 2019. 6, 7
- [59] Z. Zhang, Z. Cui, C. Xu, Y. Yan, N. Sebe, and J. Yang. Pattern-Affinitive Propagation Across Depth, Surface Normal and Semantic Segmentation. In *CVPR*, 2019. 2
- [60] H. Zhao, J. Shi, X. Qi, X. Wang, and J. Jia. Pyramid Scene Parsing Network. In *CVPR*, 2017. 5
- [61] L. Zwald and S. Lambert-Lacroix. The Berhu Penalty and the Grouped Effect. 2012. 2